THE UNIVERSITY *of* EDINBURGH

Edinburgh Research Explorer

Computer simulations of surface deposition of amphiphilic diblock copolymers driven by solvent evaporation

OPEN ACCESS

Computer simulations of surface deposition of amphiphilic diblock copolymers driven by solvent evaporation**†

D.S. Wood,[1] V. Koutsos[2] and P.J. Camp[1],*

[1]EaStCHEM, School of Chemistry, Joseph Black Building, University of Edinburgh, West Mains Road, Edinburgh, EH9 3JJ, UK.

[2]School of Engineering, University of Edinburgh, Mayfield Road, Edinburgh EH9 3JL, Scotland, UK.

[*]Corresponding author; e-mail: philip.camp@ed.ac.uk

Supporting information:
Electronic supplementary information (ESI) available: Two movies showing different views (above the surface and below the surface) of the complete simulation process. See
http://dx.doi.org/10.1039/C3SM27837A

Graphical abstract:

SOLVENT EVAPORATION
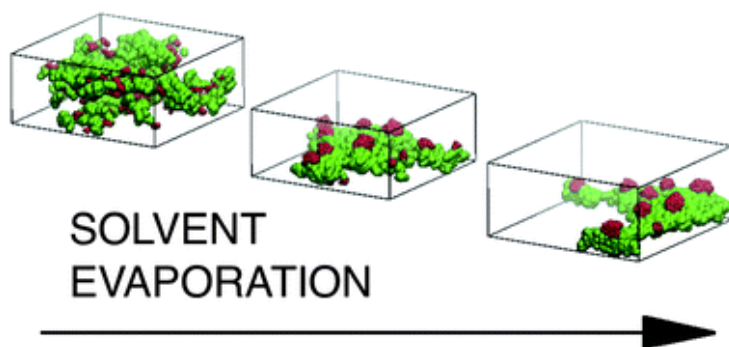
Summary:
Simulations reveal the effects of molecular architecture and solvent quality on the deposition of diblock copolymers on smooth surfaces driven by solvent evaporation.

Abstract

Large-scale molecular dynamics simulations are used to study thin films of diblock-copolymer solutions drying on a flat, smooth surface. The solution is represented by coarse-grained models of the polymers dissolved in an explicit 'atomic' solvent. The adsorption of polymers on to a flat surface is examined as the solvent slowly evaporates from the thin film. The polymer structures during and after the evaporation are compared with experimental data from atomic force microscopy measurements [E. Glynos *et al.*, *Macromolecules*, 2008, **41**, 4313–4320]. Because such processes are 'slow', we have used a bespoke molecular dynamics code utilizing GPU acceleration in order to simulate large system sizes over long timescales. The simulations show excellent qualitative agreement with experiments, and yield significant microscopic insights on the coupling between drying and adsorption.

1. Introduction

Polymers have become ubiquitous in everyday life with applications including fibres, textiles, packaging materials, surface coatings (controlling function, friction, and adhesion), medical devices, and fluid modifiers. The adaptability of polymers stems from the ability to tune freely the molecular characteristics (chemical identity and molecular architecture) in order to generate desired behaviour and responses under a given set of physical conditions. Block copolymers are examples of such materials. The functionality of block copolymers stems from the possibility of each block reacting differently to the environment, giving rise to complex structures and responses that depend on external factors such as pH[1,2] and exposure to solvents.[3] Specific interest in thin films of polymers is growing due to their use in areas as diverse as nanostructured materials[4,5] and biotechnology.[6]

The formation and structure of thin films of linear homopolymers,[7–12] star homopolymers,[13] heteroarm star polymers,[14] and diblock[15–19] and triblock[20] copolymers have been studied experimentally. These studies have covered chemisorbed and physisorbed polymers, and have been concerned with single-molecule properties such as the coil–globule transition, and thin-film properties such as friction. The focus here will be on the adsorption of polymers on to surfaces from solution, and the subsequent structural reorganisation of the polymers upon solvent evaporation. As such, the focus is on the *mechanism* by which polymers physisorb and subsequently collapse on to the surface to form the thin film. A typical experimental protocol for the study of such processes is to immerse a clean surface (such as mica or highly ordered pyrolytic graphite) in to a polymer solution – typically in good-solvent conditions – and to reach equilibrium adsorption. Then, the surface is removed and rinsed with solvent, and the excess solvent is removed by rapid drying in a gas stream. Finally, the organisation and structure of the polymers are investigated using a surface technique such as atomic-

force microscopy (AFM). In recent studies by our groups, this protocol has been used to study, in detail, the adsorption of linear homopolymers,[12] star homopolymers[13] and diblock copolymers[19] on to mica surfaces. A significant result from these studies is that the basic effect of solvent evaporation is to switch from good-solvent to bad-solvent conditions. This means that the steady-state polymer structures after solvent evaporation are related to the structures that exist in good-solvent conditions; the polymers undergo collapse and clustering due to the change in effective monomer–monomer interactions. There is no experimental evidence for polymers being redistributed on the surface by the solvent layer due to mechanisms such as spinodal dewetting[21–25] or hole nucleation.[21,22,26] These mechanisms would give rise to characteristic large-scale structures on the surface and specific variations with molecular weight that are not observed in the experiments.[12,13,19] This is one topic that can now be addressed using molecular simulations.

Experimental studies of polymer adsorption and polymer thin films yield some insight on the dominant molecular-scale mechanisms, but these have to be inferred from steady-state structures after adsorption and structural ordering have taken place. Although these processes are 'slow' from a computational standpoint, some insights can be gained from molecular simulations. The structure and dynamics of adsorbed linear homopolymers on surfaces have been studied in great detail: the literature is vast, with the key work being performed with off-lattice, bead-spring models,[27–32] although more accurate coarse-grained parametrisations are available for a variety of polymer systems.[33,34] Simple bead-spring models give access to long lengthscales and timescales, while retaining a significant degree of chemical resolution and realism in the polymer molecular structure. To complement the experimental work performed in our groups on linear homopolymers[12] and star homopolymers,[13] simulation work has been carried out in order to make a direct link with AFM measurements and to gain insights on the molecular-scale details of polymer adsorption.[35,36] In these studies, Langevin dynamics simulations of bead-spring models have been used to correlate the experimental measurements with molecular characteristics such as polymer size and functionality, solvent quality, and surface interactions. The solvent in these simulations was implicit, being represented only by the effective monomer–bead interactions, and random Brownian forces and Stokes-law drag acting on the beads. The effects of solvent evaporation were mimicked by switching the monomer–bead interactions from the appropriate good-solvent (repulsive) to bad-solvent (attractive) forms. In this study, computer simulations of diblock copolymer adsorption are performed to gain insight on the experimental measurements reported in Ref. 19. In a departure from earlier simulation work, the solvent is represented explicitly, albeit with a simplified 'atomic' model. This allows a more faithful representation of the solvent-evaporation process, and gives an accurate picture of the solvation and structure of the physisorbed polymer molecules. The associated increase in computational cost is offset by exploiting GPU acceleration with a bespoke molecular-dynamics code.

The results of Ref. 19 are summarised as background to the current simulation study. Poly(isoprene-*b*-ethylene oxide) (PI-PEO) diblock copolymers were synthesised with 29 wt% PI, corresponding to a PI monomer fraction of $x_{PI} = 0.21$. The weight-average molecular mass was 20 700 g mol^{-1}. Solutions of these polymers were adsorbed on to freshly cleaved mica surfaces, which were rinsed and dried under a stream of nitrogen. The sample was then imaged using AFM in tapping mode. The PI-PEO diblock copolymers were seen initially to form flat polymer islands which were weakly adsorbed on the substrate. They then displayed an exponential-type growth of height with time with their lateral shape becoming circular. One possible explanation for this behaviour is a change in the affinity of mica to water, and a concomitant decrease in the thickness of the water layer due to evaporation.

It has been shown that in ambient air, mica adsorbs water from the environment[37–43] and this adsorbed water is shown to form two layers. The first is a structured layer about 0.2 nm thick,[39,40] denoted 'phase I', and a thicker, bulk-like layer ranging from a monolayer to approximately 2 nm thick,[38–41] denoted 'phase II'. The affinity of mica to water decreases with time due to processes such as the adsorption of organic contaminants that are always present under ambient conditions.[40,42]

The PEO blocks of the synthesised block copolymers are hydrophilic and are expected to extend into both the phase I and phase II layers. The PI blocks are hydrophobic and are thought to be floating on top of the phase II layer. This structure corresponds to the flat islands seen at short times. As the mica becomes less hydrophilic with time, the water layer thins and hence the PEO blocks are confined to a smaller volume within phase II. As a result, the PEO blocks on the edge of the island are forced to spread laterally within the phase-I layer and in contact with the surface. The PI blocks remained floating on top of the diminished phase-II layer in a smaller 'cap'. This process is thought to give rise to the long-time growth in height. The effects of the water layer on diblock copolymers under ambient conditions have been reported before.[44–46]

The aims of this work are to reproduce and gain insight on the effect of the solvent evaporation on the structure of diblock copolymers adsorbed on surfaces such as mica, and to explore the approach to steady-state conditions, which may not necessarily be at thermodynamic equilibrium. Techniques such as Monte Carlo simulations of lattice models provide valuable information on the equilibrium structures and thermodynamics of block-copolymer systems,[47,48] but they cannot capture the complex dynamical processes that are expected to be important in the current situation. Instead, off-lattice, bead-spring models of polymers in an explicit 'atomic' solvent are studied using molecular dynamics (MD) simulations. Using a simulation protocol consisting of equilibrium, evaporation, and steady-state phases, the effects of the polymer architecture (PI : PEO ratio) and solvent selectivity are surveyed systematically. Although not yet explored in the experiments,[19] these parameters are easily varied in simulations. The results clarify the roles played by the solvent in the polymer deposition process.

This remainder of this paper is organised as follows. Section 2 contains details of the coarse-grained polymer and solvent models, and the simulation methods. The results for diblock copolymers with different block lengths in both selective and non-selective solvents are presented in Section 3, and Section 4 concludes the paper.

2. Simulation and model methods

The study of the system described above poses a significant computational challenge due to the large number of particles necessary for an explicit solvent. The explicit solvent is itself necessary, as an important part of the studied system is the liquid layer and its evaporation. The inclusion of an interface with the evaporation of the solvent leads to long computation times as systems at coexistence equilibrate slowly.[49] In order to deal with this, a bespoke code has been developed to make use of the computational power of NVIDIA GPUs *via* the language extension CUDA for C. This allows large simulations to be carried out for many millions of timesteps in a reasonable amount of time, on the order of a week. In this section we outline the model used and the simulation protocol.

2.1. Molecular models

The PI-PEO/solvent/mica system is modelled as follows. The PI units are hydrophobic while the PEO units are hydrophilic. Hence, the PEO units should have a more significant attraction to the mica surface. If the solvent is water, then it will have a strong attraction to the PEO units and the surface, but the PI–water interaction will be less favorable; in this sense, the solvent is *selective*. One might conceive of another solvent that has no strong preference for PI or PEO; this will be referred to as a *non-selective* solvent. In either case, the solvent molecules experience mutually attractive interactions.

A useful approach when considering systems of linear polymers is to model them as chains of coarse-grained beads connected by springs.[50] Each model diblock copolymer is comprised of N_b beads of equal mass, m, connected by non-linear finitely extensible (FENE) 'springs' defined by the potential

$$u_{FENE}(r) = -\frac{1}{2}kR_0^2 \ln\left(1 - \frac{r^2}{R_0^2}\right)$$

(1)

where r is the bonded bead–bead separation, R_0 is the maximum possible bead–bead separation, and k is a spring constant. The beads in each polymer may either be of type A (hydrophobic, *e.g.*, PI) or of type B (hydrophilic, *e.g.*, PEO). The solvent is represented as a system of single beads of type C. The

different chemical identities of these beads are represented by the non-bonded interactions, all of which are expressed in terms of the Lennard-Jones (LJ) potential

$$u_{LJ}(r) = 4\varepsilon \left[\left(\frac{\sigma}{r} \right)^{12} - \left(\frac{\sigma}{r} \right)^{6} \right]$$

(2)

where ε and σ are energy and range parameters, respectively. Attractive bead–bead interactions are given by the cut-and-shifted potential $u_{att}(r \leq r_c) = u_{LJ}(r) - u_{LJ}(r_c)$ and $u_{att}(r > r_c) = 0$, with $r_c = 2.5\sigma$. In a similar way, repulsive bead–bead interactions are defined by the Weeks–Chandler–Andersen

potential[51] $u_{rep}(r \leq r_0) = u_{LJ}(r) - u_{LJ}(r_0)$ and $u_{rep}(r > r_0) = 0$, where $r_0 = \sqrt[6]{2}\sigma$ is at the minimum of $u_{LJ}(r)$. In all cases, the A–A, B–B, C–C, and B–C interactions are attractive, and the A–B interaction is repulsive. In a selective solvent, the A–C interaction is repulsive, while in a non-selective solvent it is attractive.

The surface was taken to be structureless, parallel to the xy plane, and with $z < 0$. The bead–surface interactions were dealt with through an effective potential[52] based on integrating the LJ interactions with a homogeneous distribution of sites within the surface. This is given by

$$\phi(z) = \frac{2\pi\varepsilon_s}{3} \left[\frac{2}{15} \left(\frac{\sigma}{z} \right)^{9} - \left(\frac{\sigma}{z} \right)^{3} \right]$$

(3)

where z is the perpendicular distance of the bead from the surface and ε_s controls the strength of the bead surface attraction. Attractive bead–surface interactions are given by $\phi_{att}(z) = \phi(z)$, while repulsive bead–surface interactions are given by $\phi_{rep}(z \leq z_0) = \phi(z) - \phi(z_0)$ and $\phi_{rep}(z > z_0) = 0$, where the cut-off $z_0 = \sqrt[6]{2/5}\sigma$ is at the minimum of $\phi(z)$. In all cases, the interaction between A beads and the surface is repulsive, while B beads and C beads experience attractive interactions with the surface. The interaction potentials for selective and non-selective solvents are summarised in Table 1. The only difference between the two solvents is the interaction between A beads and C beads: in a selective solvent, this interaction is repulsive; in a non-selective solvent, this interaction is attractive.

Selective solvent					Non-selective solvent			
	A	B	C	S	A	B	C	S
A	$u_{att}(r)$	$u_{rep}(r)$	$u_{rep}(r)$	$\phi_{rep}(z)$	$u_{att}(r)$	$u_{rep}(r)$	$u_{att}(r)$	$\phi_{rep}(z)$
B		$u_{att}(r)$	$u_{att}(r)$	$\phi_{att}(z)$		$u_{att}(r)$	$u_{att}(r)$	$\phi_{att}(z)$
C			$u_{att}(r)$	$\phi_{att}(z)$			$u_{att}(r)$	$\phi_{att}(z)$

Table 1. Table of interactions for beads of type A (solvophobic), B (solvophilic), and C (solvent), and the surface S. For interactions between beads A–C, $u_{att}(r)$ is the Lennard-Jones (12,6) potential cut-and-shifted at $r = 2.5\sigma$, and $u_{rep}(r)$ is the Lennard-Jones (12,6) potential cut-and-shifted at the minimum $r = \sqrt[6]{2}\sigma$ (the WCA potential). For interactions involving the surface, S, $\phi_{att}(z)$ is the attractive (9,3) potential, and $\phi_{rep}(z)$ is the (9,3) potential cut-and-shifted at the minimum $z = \sqrt[6]{2/5}\sigma$

Each polymer consisted of $N_b = 50$ beads. Polymers with formula $A_{12}B_{38}$ and monomer fractions $x_A = 0.24$ and $x_B = 0.76$ approximate the polymers studied in Ref. 19 with $x_{PI} = 0.21$ and $x_{PEO} = 0.79$. Two more molecular architectures were studied, with formulas $A_{25}B_{25}$ and $A_{38}B_{12}$. For simplicity, ε_s was set equal to ε. The FENE parameters were $R_0 = 1.5\sigma$ and $\kappa = 30\varepsilon\sigma^{-2}$. Molecular dynamics simulations were performed in the NVT ensemble using a chain of Nosé–Hoover thermostats, as described by Martyna *et al.*[53] The equations of motion were integrated using the velocity-Verlet scheme[54] with timestep $\delta t/\tau = 0.002$, where $\tau = \sqrt{m\sigma^2/\varepsilon}$ is the basic unit of time. In all cases, the target temperature was $T^* = k_B T/\varepsilon = 0.8$. This is below the vapour–liquid critical temperature of a bulk atomic fluid with interaction potential $u_{att}(r)$: the critical density is $\rho_c\sigma^3 = 0.3211(5)$ and the critical temperature is $T^*_c = 1.0795(2)$.[55]

2.2. Simulation protocol

All simulations were carried out with $N_p = 100$ polymers (giving a total number of polymer beads $N_A + N_B = 5000$) and $N_C = 27\,768$ solvent beads in an $L \times L \times H$ cuboidal box. Periodic boundary conditions (PBCs) were applied in the x and y directions. All bead interactions with the 'top' surface of the box ($z > H$) were made repulsive. Following a high-temperature randomisation at $T^* = 2$, the temperature was reduced to $T^* = 0.8$. At $T^* = 0.8$ the bulk coexistence densities for the vapour and liquid phases are $\rho\sigma^3 \simeq 0.029$ and 0.73, respectively.[56–58] L was made greater than the total length of the polymers to simplify the initial crystalline packing of the system and to avoid PBC artifacts. Initial values of $L = 70\sigma$ and $H = 27.5\sigma$ were chosen to give a liquid layer of sufficient thickness to solvate the polymers, in equilibrium with a thick layer of vapour to eliminate the effects of the box boundary:

the total density of solvent beads was $\rho\sigma^3 = 0.206$; from the lever rule, and assuming bulk coexistence, this gives liquid and vapour layers approximately 7σ and 20σ thick, respectively.

For each polymer type, the simulation consisted of four distinct stages. (a) (High-temperature randomisation) initially, a short run ($\sim 7 \times 10^4$ timesteps) at a high temperature of $T^* = 2$ was carried out in order to reduce any artifacts introduced by the initial configuration. (b) (Equilibrium) The system was equilibrated at $T^* = 0.8$ over a long period of $\sim 2 \times 10^6$ timesteps ($\sim 4000\tau$). (c) (Evaporation) Evaporation was carried out by increasing H incrementally at a rate of 0.05% per 100 timesteps over $\sim 2 \times 10^5$ timesteps ($\sim 400\tau$). (d) (Steady state) The system was then maintained under constant conditions until an apparent steady-state structure was reached. Simulation snapshots from the equilibrium and steady-state stages of simulations of $A_{12}B_{38}$ polymers in selective and non-selective solvents are shown in Figure 1(a)–(d). Although the simulated molecules and system dimensions are small compared to those in experiments, they should give a qualitative picture of the dominant molecular-scale processes.

(a) $A_{12}B_{38}$ SS: equilibrium   (b) $A_{12}B_{38}$ NS: equilibrium

(c) $A_{12}B_{38}$ SS: steady state   (d) $A_{12}B_{38}$ NS: steady state

(e) $A_{25}B_{25}$ SS: steady state   (f) $A_{25}B_{25}$ NS: steady state

(g) $A_{38}B_{12}$ SS: steady state   (h) $A_{38}B_{12}$ NS: steady state
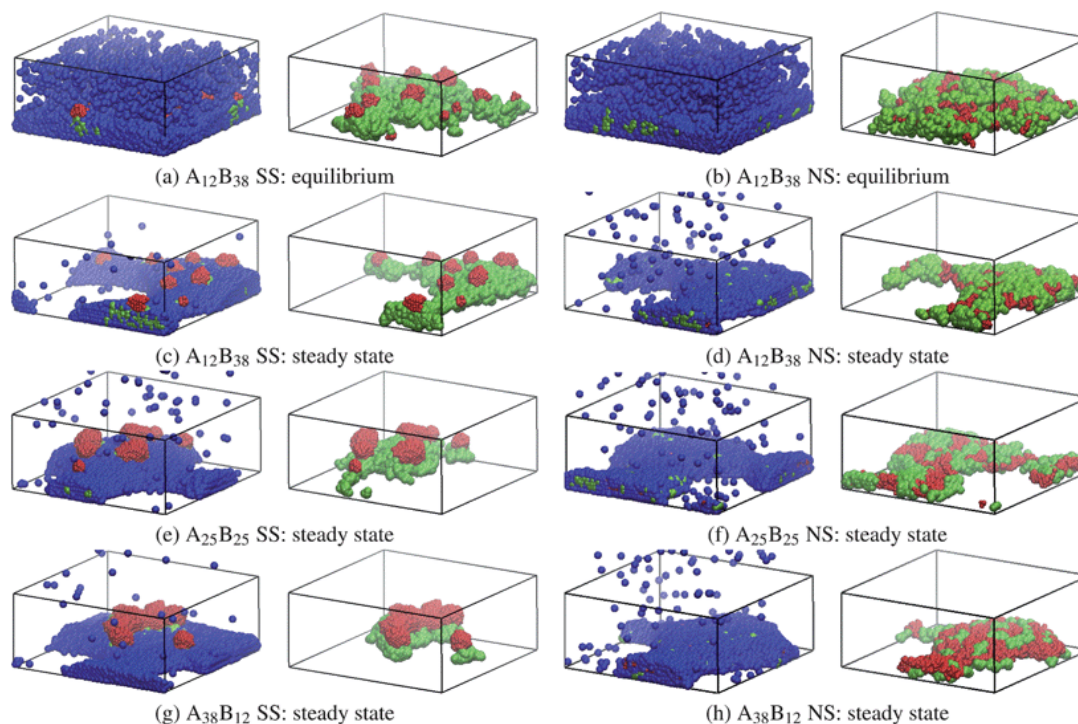
Figure 1. Snapshots from simulations of polymers in a selective solvent (SS) (a, c, e and g) and non-selective solvent (NS) (b, d, f and h) at $T^* = 0.8$: (a and b) equilibrium; (c–h) steady-state conditions after evaporation. A beads are red, B beads are green, and C beads (solvent) are blue. In each case, snapshots are shown with and without solvent included. The box dimensions are those during the equilibrium stages of the simulations.

Movies of the complete simulations are provided in the ESI.‡ The example given is of $A_{12}B_{38}$ in selective solvent. The equilibrium period extends up to time 1 min 5 s. Then the solvent begins to evaporate, and solvent dewetting is seen to occur at around 1 min 10 s. As a result, polymer clusters go on to aggregate further and the structure coarsens. In the movies, one can see a typical process of two polymer clusters being driven together by solvent dewetting. Views from above and below the surface are provided. This mechanism is elucidated in Section 3.

3. Results

In each of Sections 3.1–3.4, results are shown for each of the polymer architectures ($A_{12}B_{38}$, $A_{25}B_{25}$, $A_{38}B_{12}$), and for selective and non-selective solvents.

3.1. Equilibrium density profile

Figure 2 shows the local density of each bead at equilibrium, prior to solvent evaporation. In each case, the solvent forms a liquid-like layer near the surface. The local solvent density shows strong layering near the surface, and with increasing distance z shows damped oscillations around an average density of about $\rho\sigma^3 \simeq 0.6$, before falling rapidly as the liquid–vapour interface is traversed. By fitting a simple interfacial profile

$$\rho(z) = \frac{1}{2}\left(\rho_{vap} + \rho_{liq}\right) + \frac{1}{2}\left(\rho_{vap} - \rho_{liq}\right)\tanh\left(\frac{z - z_i}{\xi}\right)$$

(4)

which ignores the oscillations near to the surface, rough estimates can be obtained for the average vapour and liquid densities ρ_{vap} and ρ_{liq}, and the position (z_i) and width (ξ) of the interface. These are given in Table 2 and the fits are shown in Figure 2. The apparent vapour and liquid densities are different from their bulk values due to the presence of the polymers and the surfaces. z_i can be identified with the thickness of the liquid–solvent layer, which is around 8–9σ in each case, and slightly higher than that expected from the lever rule due to the solvation of the polymers. It is important to note that ξ is the apparent interfacial width only for the specific system size being considered. From simulations of polymer mixtures in slit-pores, Werner *et al.* found very significant finite-size effects where the concentration profile varied strongly not only with the confined-film thickness, but also with the lateral dimension of the simulation cell (corresponding to L here).[59,60] This is, in fact, a general feature of interfaces between phases at coexistence, arising from capillary-wave broadening.[61]
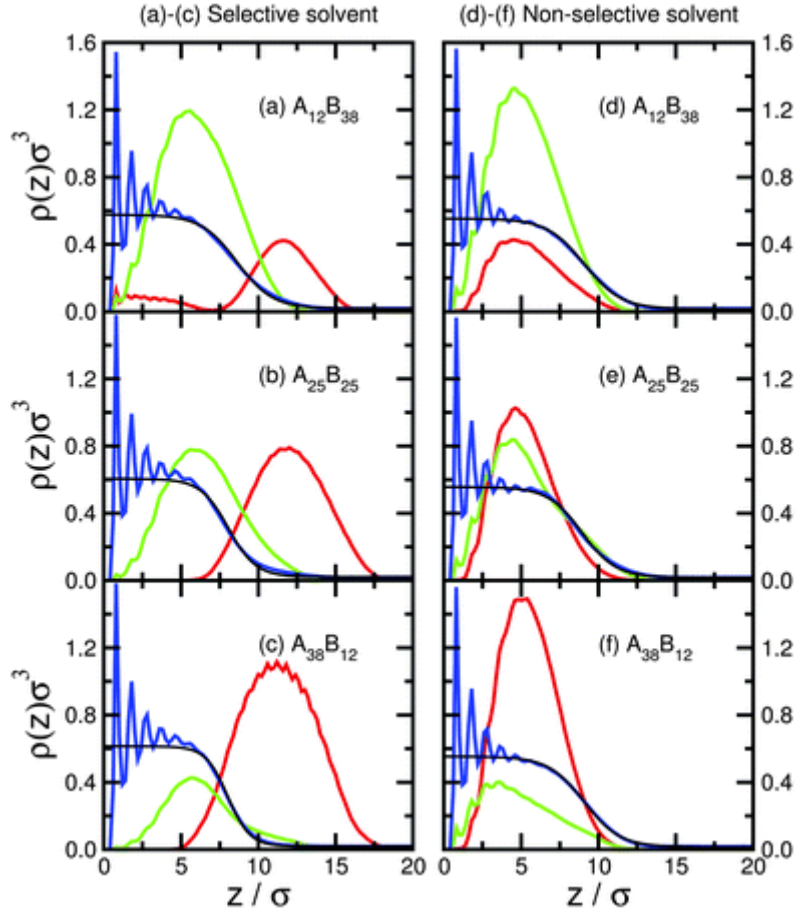
Figure 2. Local density $\rho(z)$ during the equilibrium stage for A beads (red), B beads (green), and solvent (C) beads (blue). The densities $\rho_A(z)$ and $\rho_B(z)$ have been multiplied by 10 for clarity. The thin black lines are fits to the solvent density using eqn (4). Results are shown for a selective solvent (a–c) and for a non-selective solvent (d–f).

System	$\rho_{vap}\sigma^3$	$\rho_{liq}\sigma^3$	z_i/σ	ξ/σ
$A_{12}B_{38}$/SS	0.018(15)	0.576(28)	8.60(33)	2.31(58)
$A_{25}B_{25}$/SS	0.021(15)	0.605(27)	8.05(28)	1.79(48)
$A_{38}B_{12}$/SS	0.019(15)	0.614(26)	8.02(24)	1.43(41)
$A_{12}B_{38}$/NS	0.015(15)	0.553(27)	9.07(35)	2.40(61)
$A_{25}B_{25}$/NS	0.018(15)	0.556(26)	8.93(33)	2.19(57)
$A_{38}B_{12}$/NS	0.015(15)	0.553(26)	9.07(34)	2.31(59)

Table 2. Estimates of the vapour–liquid interfacial properties of the solvent at equilibrium: ρ_{vap} and ρ_{liq} are the vapour and liquid densities, respectively, z_i is the position of the interface, and ξ is the interfacial width, all as fitted by eqn (4). 'SS' and 'NS' denote selective and non-selective solvents, respectively.

The A and B beads are distributed according to the selectivity of the solvent. With a selective solvent, the solvophilic B beads are located preferentially near the surface, while the solvophobic A beads are expelled from the liquid layer. With a non-selective solvent, the A and B density profiles are similar, with peak positions in the region of $z = 5\sigma$. The B beads show a little more structure near the surface due to the attractive interactions with the surface. Snapshots of $A_{12}B_{38}$ polymers equilibrated in selective and non-selective solvents are shown in Figure 1(a) and (b), respectively. In selective solvent, the polymers form structures where the solvophobic A beads are clustered together to form caps that 'float' on the islands formed by the B beads. In non-selective solvent, the A beads are still clustered, but these clusters are dispersed within the layer of B beads. The repulsive interactions between A beads and selective-solvent beads lead to a greater degree of clustering and protrusion from the liquid layer.

The properties of the solvent layer reported in Table 2 vary weakly but systematically amongst the different cases. For a given polymer, the liquid layer is thicker, the interface is broader, and the liquid density is lower for a non-selective solvent than for a selective solvent. This is due to the full solvation of the polymer in the non-selective solvent layer. With a non-selective solvent, the properties of the liquid layer are not strongly dependent on the polymer. With a selective solvent, the liquid layer gets thicker, the interface gets broader, and the liquid density decreases as the proportion of solvophilic polymer beads is increased, reflecting the greater degree of polymer solvation.

3.2. Film height

Following the equilibration stage, the solvent is evaporated by box expansion which causes further desolvation of the polymers and their subsequent collapse on to the surface. Some observations on the mechanisms of solvent evaporation and surface dewetting will be presented in Section 3.5, but for now the focus is on the polymers. The collapse of the polymer film is reflected in the average bead height h, and those resolved in to different types of polymer beads. Figure 3 show the time dependence of h through the equilibrium, evaporation, and steady-state stages of the simulations.
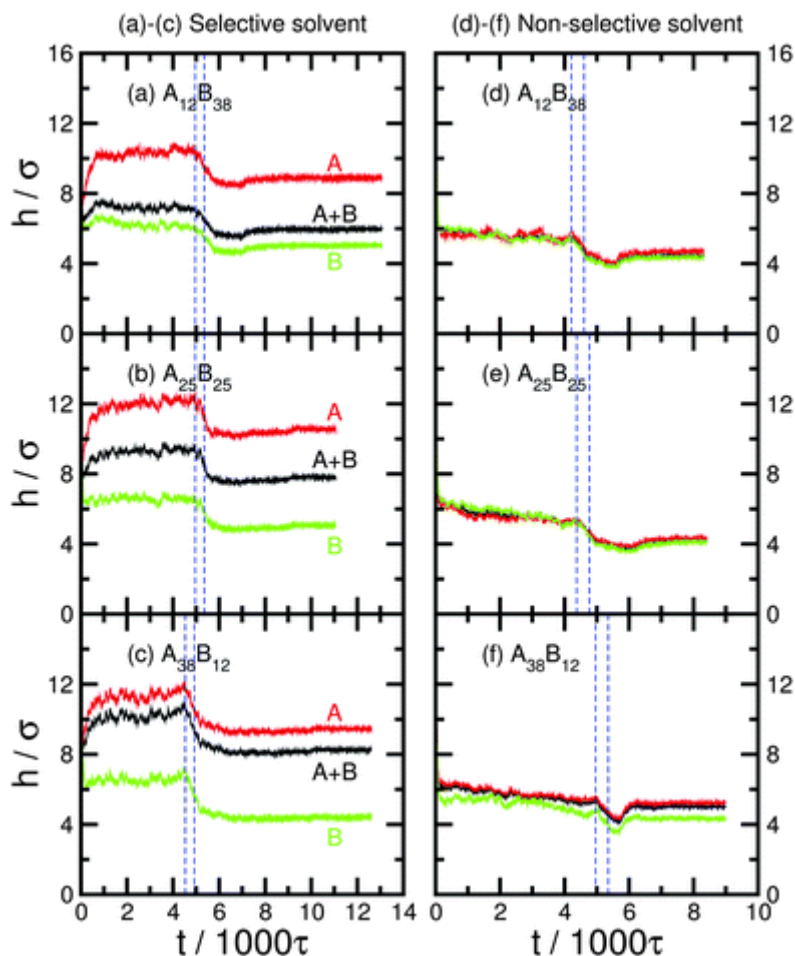
Figure 3. Average bead height *h* for A beads (red), B beads (green), and all A and B beads (black). Results are shown for a selective solvent (a–c) and for a non-selective solvent (d–f). The blue dashed lines indicate the beginning and end of the solvent-evaporation stage.

Figure 3(a)–(c) show the results for polymers in a selective solvent. In all cases, and throughout each stage of the simulation, the solvophobic A beads are further from the surface than the B beads. The average height of all beads is a simple weighted average of the A and B bead heights. Upon solvent evaporation, the bead heights drop immediately and rapidly due to thinning of the uppermost part of the liquid–solvent film. Significantly, on a longer timescale, the bead heights increase with time. This is most clear for $A_{12}B_{38}$, in which *h* shows a rather rapid increase at around $t \simeq 7000\tau$. It turns out that this is when the solvent begins to dewet the surface; solvent dewetting is discussed further in Section 3.5. The results imply that a slow decrease in the amount of adsorbed solvent causes the polymer molecules to 'pile up'. This can be compared with the slow exponential increase in height seen in experiments.[19] To underline this correspondence, Figure 4 shows a detail of the average height for $A_{12}B_{38}$, along with a suitable exponential fit.
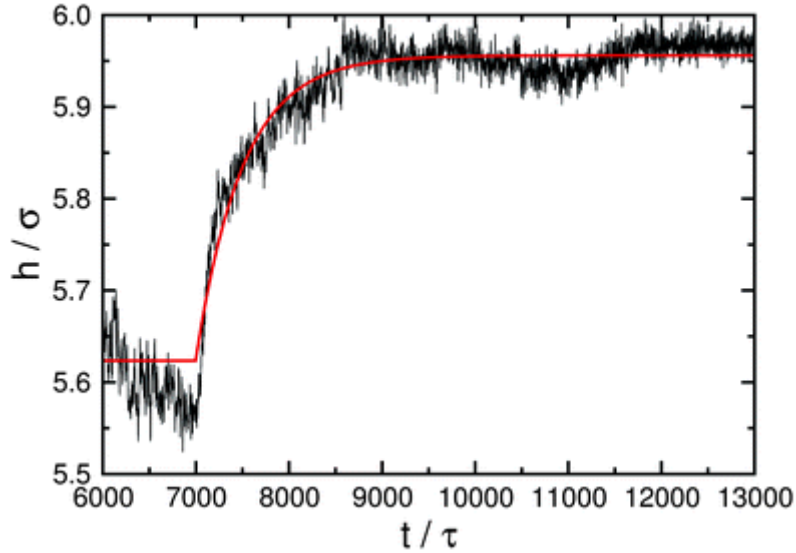
Figure 4. Average bead height h for all A and B beads in $A_{12}B_{38}$ polymers in selective solvent. The black line traces the simulation results, and the red line is a fit to the expression $h(t) = h_0 + \Delta h[1 - e^{-k(t-t_0')}]$ for $t > t_0$, where $t_0 \simeq 7000\tau$.

In each case, h eventually approaches a steady-state value. For each polymer, the average steady-state heights of the A and B beads are 9–10$\sigma$and 4–5σ, respectively. The steady-state structures of all polymers in selective solvents are shown in Figure 1(c), (e) and (g). For $A_{12}B_{38}$ polymers, a comparison of Figure 1(a) and (c) shows the overall flattening of the B beads on to the surface when the solvent has evaporated and is no longer fully wetting the surface. Figure 1(c), (e) and (g) show that, irrespective of the composition, the A beads form clustered caps that sit on top of the B beads.

Figure 3(d)–(f) show that, in a non-selective solvent, the A and B beads are dispersed evenly through the polymer layer at all times. At the start of solvent evaporation, h drops due to the depletion of the topmost part the liquid–solvent layer, but then increases again as further solvent dewetting causes beads to 'pile up'. A comparison of Figure 1(b) and (d) shows the overall flattening of $A_{12}B_{38}$ accompanying the onset of solvent evaporation.Figure 1(d), (f) and (h) show that the A beads are clustered, but that the clusters remain dispersed within the islands of B beads on the surface. The steady-state structures shown in Figure 1(d), (f) and (h) are qualitatively similar to those at the equilibrium stage.

3.3. Radius of gyration

The dimension of a single polymer is indicated by the radius of gyration R_g. A two-dimensional radius of gyration is defined as

$$R_g^2 = \left\langle \frac{1}{N^2} \sum_i^N \sum_j^N |x_i - x_j|^2 + |y_i - y_j|^2 \right\rangle$$

(5)

where the sum was either over all A beads in the polymer, all B beads in the polymer, or all beads in the polymer. This quantity gives an indication of the lateral spread of the molecules with respect to the surface (xy plane). The time dependence of R_g is shown in Figure 5. In all cases, the radii of gyration of A and B beads increase with the respective monomer fractions. For $A_{25}B_{25}$ in a selective solvent, R_g of the B beads is slightly higher than that of the A beads during equilibrium stage, presumably due to the attractive interaction between B beads and the surface, and a flattening on the surface. In non-selective solvent the A and B beads of $A_{25}B_{25}$ exhibit essentially the same radii.
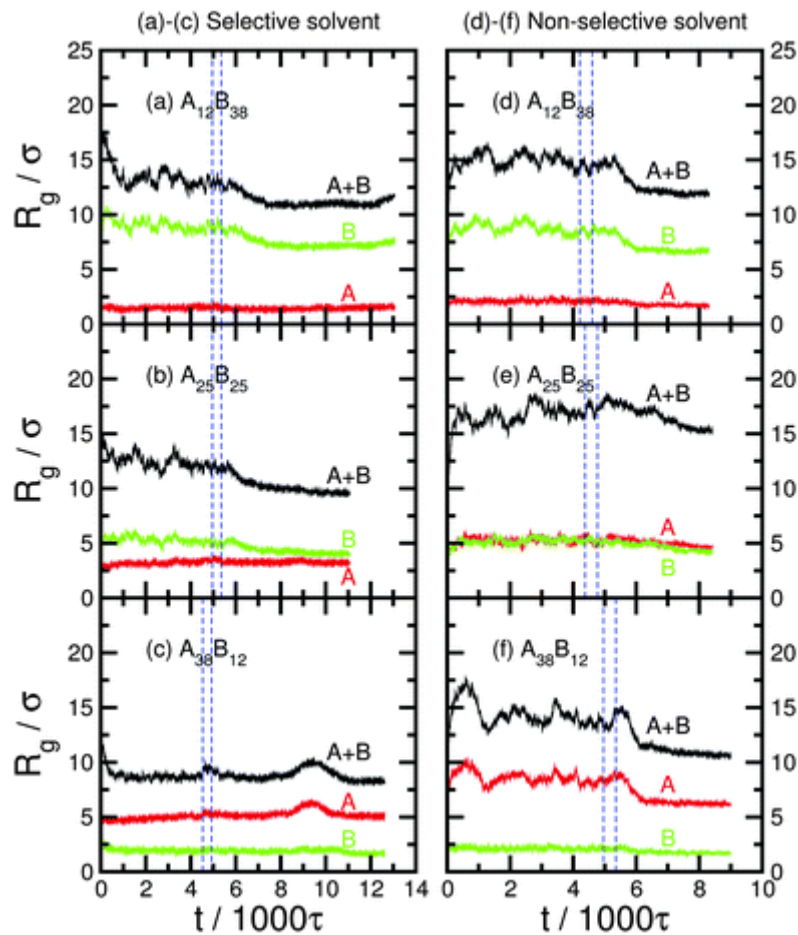

Figure 5. Two-dimensional radius of gyration R_g for A beads (red), B beads (green), and all A and B beads (black). Results are shown for a selective solvent (a–c) and for a non-selective solvent (d–f). The blue dashed lines indicate the beginning and end of the solvent-evaporation stage.

Generally, for both types of solvent, the onset of solvent evaporation leads to a rapid decrease in R_g for the majority bead type, while R_g for the minority bead type stays roughly constant. For example, in $A_{12}B_{38}$, the B beads contract laterally while the A beads – which are already clustered and perched on top of the B beads – remain much as they were. In combination with the simultaneous and rapid reduction in film height, these data indicate an overall collapse of the polymers on to the surface. On longer timescales, there is a slow decrease which correlates with the 'piling up' effect seen in the bead heights. Overall, the picture is that the conformations of individual polymers undergo rapid collapse at the onset of solvent evaporation, and afterwards decrease towards slowly steady-state values as further solvent dewetting occurs.

3.4. Characteristic length

So far, the picture is that solvent evaporation leads to an initial rapid collapse of the polymers, followed by a slow lateral contraction and 'piling up' as more of the solvent evaporates. The simulation snapshots in Figure 1 show that the polymer molecules aggregate. Coarsening in the surface plane is monitored by a characteristic length l given by[62]

$$l = \frac{2\pi}{\langle k \rangle} = \frac{2\pi \sum_k S(k)/g(k)}{\sum_k k S(k)/g(k)}$$

(6)

where $\boldsymbol{k} = 2\pi(n_x, n_y)/L$ ($n_x, n_y = 0, \pm1, \pm2, \ldots$) is a two-dimensional wavevector, $k = |\boldsymbol{k}|$, $S(\boldsymbol{k})$ is the structure factor, and $g(k)$ is the number of wavevectors with length k. $S(\boldsymbol{k})$ is given by

$$S(\boldsymbol{k}) = \rho(\boldsymbol{k})\rho(-\boldsymbol{k}) \tag{7}$$

where $\rho(\boldsymbol{k}) = \sum_{i=1}^{N} \exp(-i\boldsymbol{k}\cdot\boldsymbol{r}_i)$ is an instantaneous Fourier component of the particle density. A high-k cutoff of $2\pi/\sigma$ was applied to the sum over wavevectors. Characteristic lengths were computed separately for the A beads, the B beads, and the A and B beads combined, and the results are shown in Figure 6. The characteristic length for a given bead type increases with its monomer fraction. In non-selective solvents there is a slight downward drift in l during the equilibration stage, reflecting very slow collective relaxation to equilibrium. Upon solvent evaporation, l increases quite sharply reflecting a growing lengthscale in the xy plane. This signals that low-wavevector density correlations in the polymer film are growing as the solvent evaporates and dewets the surface. Two processes may contribute to this effect: the agglomeration of loosely associated polymers in the film; and an overall increase in the local concentration of beads within the polymers. For a given bead type, the characteristic lengths in selective and non-selective solvents are very similar to one another. There

was a fluctuation in l for the A beads in the $A_{38}B_{12}$ polymers in selective solvent [Figure 6(c)] at $t \simeq$ 9000τ. This coincides with slight jumps seen at the same time in R_g. The bead height h shows no fluctuation. These features coincided with the onset of rapid solvent evaporation, and the ultimate steady-state values appear to have been unaffected.
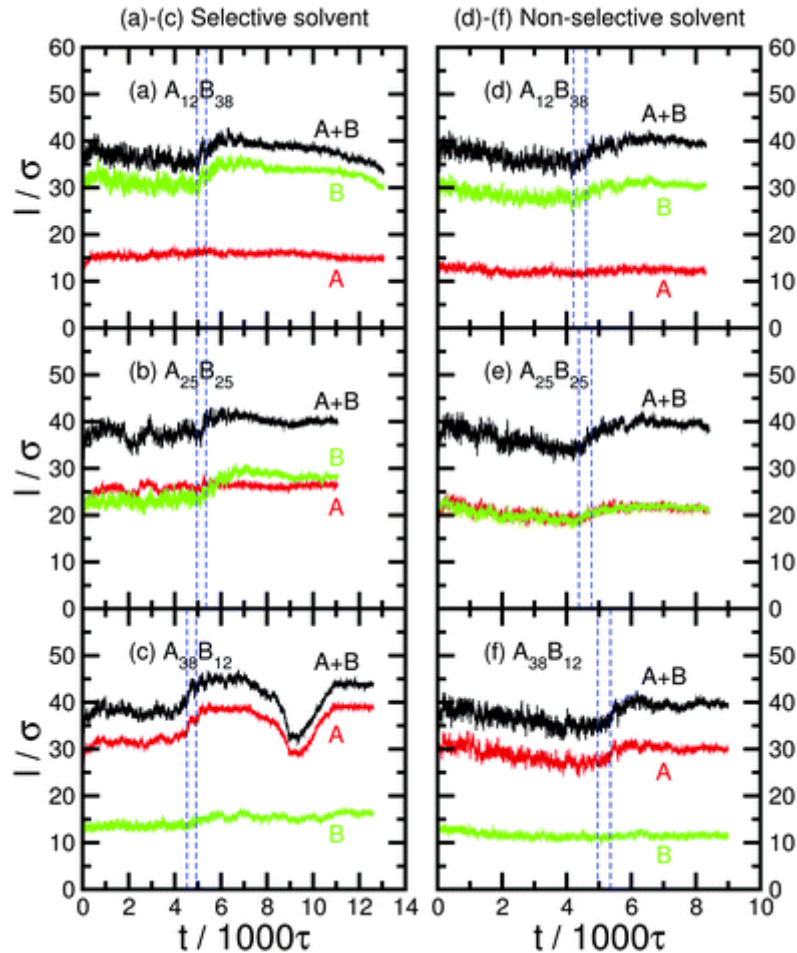

Figure 6. Characteristic length l for A beads (red), B beads (green), and all A and B beads (black). Results are shown for a selective solvent (a–c) and for a non-selective solvent (d–f). The blue dashed lines indicate the beginning and end of the solvent-evaporation stage.

3.5. Solvent evaporation, dewetting, and polymer restructuring

Figure 3–5 all show rapid responses in the structure of the polymer film at the onset of solvent evaporation, followed by slower variations as more and more solvent evaporates and eventually dewets the surface. Clearly, then, this two-stage process is tied to the evaporation mechanism of the solvent. The solvent molecules near the liquid–vapour interface begin to evaporate first, leading to a

desolvation of the top-most parts of the polymers and an immediate reduction in the film height, as shown in Figure 3. At a later stage, the solvent dewets the surface, apparently due to a heterogeneous nucleation effect since the dewetting of the surface originates on the perimeters of polymer clusters, and then spreads out. This late-stage desolvation of the polymers leads to an increase in the height h (Figure 4) and a decrease in the lateral radius of gyration R_g (Figure 5). The overall picture is that, upon solvent evaporation, the polymers first flatten rapidly, and then slowly contract laterally and increase in height. The complete process is shown in the movies provided in the ESI;‡ see Section 2.2 for an explanation. The steady-state snapshots in Figure 1(c)–(h) show that there is a residual film of solvent on the polymers, but that the bare surface is dewetted. This is only a monolayer, however, and this appears to have no further bearing on the development of the polymer structure.

4. Conclusions

Computer simulations have been used to study the deposition of amphiphilic diblock copolymers on a smooth surface driven by solvent evaporation. Coarse-grained models of the polymers were constructed to reflect different ratios of solvophilic (and 'surfacephilic') and solvophobic (and 'surfacephobic') components, including a ratio studied experimentally.[19] In contrast with earlier simulations of similar systems, the solvent was modelled explicitly, allowing an investigation of solvent quality (whether it is selective for one of the polymer components or non-selective), and the coupling between the solvent dewetting processes and polymer structure. The significant computational cost associated with the explicit solvent was offset by using a bespoke molecular-dynamics code written for GPUs.

The simulation protocol was designed to mimic the situation of the polymers solvated by a thin liquid film in equilibrium with its vapour, followed by solvent evaporation and the approach to a steady state. The structure of the thin films was elucidated by examining individual density profiles of the solvent molecules, and the solvophilic and solvophobic components of the polymers. In general, the polymers form clusters with the surfacephilic groups providing a flat base on top of which the surfacephobic groups form clusters. The evolution of the polymer structure upon solvent evaporation was monitored by measuring molecular heights, radii of gyration, and a characteristic length which characterises coarsening of the structure.

In general, the deposition mechanism upon solvent evaporation consists of two stages. The solvent molecules near the liquid–vapour interface are the first to evaporate, and this leads to an immediate flattening of the polymers. Next, the solvent dewets from the surface *via* a nucleation process originating near the perimeters of the polymer clusters. This leads to a lateral contraction and a slight

increase in the polymer height. The overall picture supports the general mechanisms put forward in Ref. 19.

This is only a first attempt at simulating polymer deposition by solvent evaporation. There are at least three effects that have not been addressed with the coarse-grained model and simulation protocol adopted here. Firstly, the system has been maintained at a constant temperature using an artificial thermostat, whereas in reality, a temperature gradient would be established in the polymer–solvent film due to evaporative cooling by the solvent. Secondly, the coarse-grained model is a very crude representation of the various interactions between polymer, surface, and solvent. There are several specific, chemical details that may play significant roles in the polymer deposition process, including the structure and hydration of the surface, the cause of solvent evaporation from the surface, and the precise changes in interactions as the polymers crossover from good-solvent to bad-solvent conditions upon solvent evaporation. Thirdly, given the limitations on simulation lengthscale and timescale, it has not been possible to survey the effects of varying the rate of solvent evaporation with respect to polymer relaxation rates: this could well be a parameter that influences the structure of the adsorbed polymer film. These factors may be addressed in future work.

Despite these limitations, and the fact that the simulations are unavoidably limited to short lengthscales and timescales, the results show how solvent evaporation can control the slow restructuring of diblock copolymers on a surface, which is precisely the effect measured in experiments.[19]

References

[1] G. B. Webber, E. J. Wanless, V. Bütün, S. P. Armes and S. Biggs, *Nano Lett.*, 2002, **2**, 1307–1313.

[2] G. B. Webber, E. J. Wanless, S. P. Armes, Y. Tang, Y. Li and S. Biggs, *Adv. Mater.*, 2004, **16**, 1794–1798.

[3] C. Xu, X. Fu, M. Fryd, S. Xu, B. B. Wayland, K. I. Winey and R. J. Composto, *Nano Lett.*, 2006, **6**, 282–287.

[4] C. Park, J. Yoon and E. L. Thomas, *Polymer*, 2003, **44**, 6725–6760.

[5] O. K. C. Tsui and T. B. Russell, *Polymer thin films*, World Scientific, New Jersey, 2008.

[6] H. L. Khor, Y. Kuan, H. Kukula, K. Tamada, W. Knoll, M. Moeller and D. W. Hutmacher, *Biomacromolecules*, 2007, **8**, 1530–1540.

[7] V. Koutsos, E. W. van der Vegte, E. Pelletier, A. Stamouli and G. Hadziioannou, *Macromolecules*, 1997, **30**, 4719–4726.

[8] V. Koutsos, E. W. van der Vegte, P. C. M. Grim and G. Hadziioannou, *Macromolecules*, 1998, **31**, 116–123.

[9] V. Koutsos, E. W. van der Vegte and G. Hadziioannou, *Macromolecules*, 1999, **32**, 1233–1236.

[10] A. Kiriy, G. Gorodyska, S. Minko, W. Jaeger, P. Štěpánek and M. Stamm, *J. Am. Chem. Soc.*, 2002, **124**, 13454–13462.

[11] S. Minko, A. Kiriy, G. Gorodyska and M. Stamm, *J. Am. Chem. Soc.*, 2002, **124**, 3218–3219.

[12] E. Glynos, A. Chremos, P. J. Camp, E. Theofanidou and V. Koutsos, in preparation.

[13] E. Glynos, A. Chremos, G. Petekidis, P. J. Camp and V. Koutsos, *Macromolecules*, 2007, **40**, 6947–6958.

[14] A. Kiriy, G. Gorodyska, S. Minko, M. Stamm and C. Tsitsilianis, *Macromolecules*, 2003, **36**, 8704–8711.

[15] J. C. Meiners, A. Quintel-Ritzi, J. Mlynek, H. Elbs and G. Krausch, *Macromolecules*, 1997, **30**, 4945–4951.

[16]   J. P. Spatz, M. Möller, M. Noeske, R. J. Behm and M. Pietralla, *Macromolecules*, 1997, **30**, 3874–3880.

[17]   J. Kumaki and T. Hashimoto, *J. Am. Chem. Soc.*, 2003, **125**, 4907–4917.

[18]   J. C. Zhao, S. Z. Tian, Q. Wang, X. B. Liu, S. C. Jiang, X. L. Ji, L. An and B. Z. Jiang, *Eur. Phys. J. E*, 2005, **16**, 49–56.

[19]   E. Glynos, S. Pispas and V. Koutsos, *Macromolecules*, 2008, **41**, 4313–4320.

[20]   X. Li, Y. C. Han and L. An, *Langmuir*, 2002, **18**, 5293–5298.

[21]   R. Seemann, S. Herminghaus and K. Jacobs, *Phys. Rev. Lett.*, 2001, **86**, 5534–5537.

[22]   R. Seemann, S. Herminghaus and K. Jacobs, *J. Phys.: Condens. Matter*, 2001, **13**, 4925–4938.

[23]   E. Ruckenstein and R. K. Jain, *J. Chem. Soc., Faraday Trans. 2*, 1974, **70**, 132–147.

[24]   G. Reiter, A. Sharma, A. Casoli, M.-O. David, R. Khanna and P. Auroy, *Langmuir*, 1999, **15**, 2551–2558.

[25]   A. Sharma and R. Khanna, *J. Chem. Phys.*, 1999, **110**, 4929–4936.

[26]   U. Thiele, M. Mertig and W. Pompe, *Phys. Rev. Lett.*, 1998, **80**, 2869–2872.

[27]   A. Milchev and K. Binder, *Macromolecules*, 1996, **29**, 343–354.

[28]   K. Binder, A. Milchev and J. Baschnagel, *Annu. Rev. Mater. Sci.*, 1996, **26**, 107–134.

[29]   N. Källrot and P. Linse, *Macromolecules*, 2007, **40**, 4669–4679.

[30]   N. Källrot, M. Dahlqvist and P. Linse, *Macromolecules*, 2009, **42**, 3641–3649.

[31]   P. Linse and N. Källrot, *Macromolecules*, 2010, **43**, 2054–2068.

[32]   P. Linse, *Soft Matter*, 2012, **8**, 5140–5150.

[33]   G. Srinivas, D. E. Discher and M. L. Klein, *Nat. Mater.*, 2004, **3**, 638–644.

[34]   P. Carbone, H. A. K. Varzaneh, X. Y. Chen and F. Müller-Plathe, *J. Chem. Phys.*, 2008, **128**, 064904.

[35]   A. Chremos, E. Glynos, V. Koutsos and P. J. Camp, *Soft Matter*, 2009, **5**, 637–645.

[36]   A. Chremos, P. J. Camp, E. Glynos and V. Koutsos, *Soft Matter*, 2010, **6**, 1483–1493.

[37]   J. Israelachvili and R. Pashley, *Nature*, 1982, **300**, 341–342.

[38]   D. Beaglehole and H. K. Christenson, *J. Phys. Chem.*, 1992, **96**, 3395–3404.

[39]   J. Hu, X. D. Xiao, D. F. Ogletree and M. Salmeron, *Science*, 1995, **268**, 267–269.

[40]   J. Hu, X. D. Xiao, D. F. Ogletree and M. Salmeron, *Surf. Sci.*, 1995, **344**, 221–236.

[41]   W. Cantrell and G. E. Ewing, *J. Phys. Chem. B*, 2001, **105**, 5434–5439.

[42]   C. Spagnoli, K. Loos, A. Ulman and M. K. Cowan, *J. Am. Chem. Soc.*, 2003, **125**, 7124–7128.

[43]   L. Cheng, P. Fenter, K. L. Nagy, M. L. Schelgel and N. C. Sturchio, *Phys. Rev. Lett.*, 2001, **87**, 156103.

[44]   N. H. Thomson, *J. Microsc.*, 2005, **217**, 193–199.

[45]   N. Crampton, W. A. Bonass, J. Kirkham and N. H. Thomson, *Langmuir*, 2005, **21**, 7884–7891.

[46]   N. Crampton, W. A. Bonass, J. Kirkham and N. H. Thomson, *Ultramicroscopy*, 2006, **106**, 765–770.

[47]   T. Chen, H. Liu and Y. Hu, *J. Chem. Phys.*, 2001, **114**, 5937–5948.

[48]   M. E. Gindy, R. K. Prud'homme and A. Z. Panagiotopoulos, *J. Chem. Phys.*, 2008, **128**, 164906.

[49]   M. Mecke, J. Winkelman and J. J. Fischer, *J. Chem. Phys.*, 1997, **107**, 9264–9270.

[50]   G. S. Grest and K. Kremer, *Phys. Rev. A: At., Mol., Opt. Phys.*, 1986, **33**, 3628–3631.

[51]   J. D. Weeks, D. Chandler and H. C. Andersen, *J. Chem. Phys.*, 1971, **54**, 5237–5247.

[52]   S. W. Sides, G. S. Grest and M. J. Stevens, *Macromolecules*, 2002, **35**, 566–573.

[53]   G. J. Martyna, D. J. Tobias and M. L. Klein, *J. Chem. Phys.*, 1994, **101**, 4177–4189.

[54]   G. J. Martyna, M. E. Tuckerman, D. J. Tobias and M. L. Klein, *Mol. Phys.*, 1996, **87**, 1117–1157.

[55]   W. Shi and J. K. Johnson, *Fluid Phase Equilib.*, 2001, **187–188**, 171–191.

[56]   B. Smit, PhD thesis, Utrecht University, The Netherlands, 1990 .

[57]   B. Smit, *J. Chem. Phys.*, 1992, **96**, 8639–8640.

[58]   P. J. Camp and M. P. Allen, *Mol. Phys.*, 1996, **88**, 1459–1469.

[59]   A. Werner, F. Schmid, M. Müller and K. Binder, *J. Chem. Phys.*, 1997, **107**, 8175–8188.

[60]   A. Werner, F. Schmid, M. Müller and K. Binder, *Phys. Rev. E: Stat. Phys., Plasmas, Fluids, Relat. Interdiscip. Top.*, 1999, **59**, 728–738.

[61]   K. Binder and M. Müller, *Int. J. Mod. Phys. C*, 2000, **11**, 1093–1113.

[62]   V. M. Kendon, M. E. Cates, I. Pagonabarraga, J.-C. Desplat and P. Bladon, *J. Fluid Mech.*, 2001, **440**, 147–203.